Theoretical Analysis and Verification of Ultrasound Displacement and Strain Imaging

Andrei R. Skovoroda, Stanislav Y. Emelianov, *Member, IEEE,* Mark A. Lubinski, Armen P. Sarvazyan, *Member, IEEE,* and Matthew O'Donnell, *Fellow, IEEE*

***Abstract*—Evaluation of internal displacement and strain distributions in tissue under externally applied forces is a necessary step in elasticity imaging. To obtain a quantitative image of the elastic modulus, strain and displacement fields must be measured with reasonable accuracy and inverted based on an accurate theoretical model of soft tissue mechanics. In this paper, results of measured internal strain and displacement fields from gel-based phantoms are compared with theoretical predictions of a linear elastic model. In addition, some aspects of elasticity reconstruction based on measured displacement and strain fields are discussed.**

I. Introduction

CHANGES in soft tissue elasticity are usually related to some abnormal, pathological process. The success of palpation as a diagnostic tool is evidence of this. Even today, palpation is widely used as a self-screening procedure for hard masses in the breast and testes. Its efficacy, however, is limited to abnormalities located relatively close to the skin surface. Moreover, information obtained by palpation is inherently subjective. Nevertheless, differences in elasticity (Young's or shear modulus) between tissues can be significant [1], whereas bulk modulus variations in soft tissue, the primary contrast mechanism in current ultrasound imaging, are only a few percent [2]. Therefore, even if measurements of the elastic modulus are made with reasonable error, there is hope that imaging of tissue shear elasticity will become a new modality of significant diagnostic value [3]–[20].

There has been consistent interest in tissue elasticity, where several direct methods have been suggested to measure the mechanical properties of tissue. More recently, elasticity imaging has been proposed by a number of investigators, where convenient imaging modalities have been used to evaluate tissue motion induced by an external force/displacement source [3]–[20]. Unfortunately, no imaging modalities, including ultrasound, nuclear magnetic resonance and computed tomography, can directly provide information about tissue elasticity. Therefore, the elastic properties of tissue must be reconstructed using information obtained from conventional imaging systems.

In general, any imaging system can provide information about tissue motion [3]–[20]. One approach is to reconstruct the elastic properties of tissue based on ultrasonic measurement of tissue motion under externally applied forces. In competition with other imaging modalities, ultrasound has two major advantages for elasticity imaging: it is inherently real-time and speckle artifacts limiting the quality of conventional images provide reasonable markers for accurate tracking of tissue motion. Elasticity can be imaged by measuring tissue motion with a speckle tracking algorithm, followed by reconstruction of the elasticity distribution. Ultrasound elasticity imaging, therefore, consists of three main components: speckle or internal boundary tracking and evaluation of tissue motion, measurement of strain tensor components, and reconstruction of the spatial distribution of the elastic modulus using strain images.

Quantitative interpretation of any measured tissue response to applied force must be based on a reasonable mathematical model of tissue behavior. To date, a linear elastic model has been used [13], [16], [19]–[23]. For example, to understand surface acoustic wave characteristics and their quantitative relation to the mechanical properties of skin, a layered model of tissue on a semi-infinite half space was used in [22], [23]. With the assumption of an infinitely extended motion source, a boundary value problem was formulated in terms of only one component of the displacement and an integral solution was found and evaluated numerically. To correlate the mechanical properties of an inhomogeneous gel-based phantom with the internal distribution of vibration magnitude produced by an external low-frequency vibration source, a finite element analysis was used in [13]. A linear elasticity model has also been used to estimate the elastic properties of tissue based on experimental ultrasonic data in the static case [16], [19].

In this paper, results of measured internal strain and displacement fields from gel-based phantoms obtained with an ultrasound speckle tracking procedure described in a companion paper [24] are compared with theoretical predictions of a linear elastic model accounting for the boundary conditions of the measurement (i.e., forward problem). In addition, some aspects of elasticity reconstruction based on measured strain and displacement fields (i.e., inverse problem) and a proper theoretical model are discussed.

Manuscript received February 11, 1993; revised December 6, 1993; accepted December 8, 1993. This work was supported in part by the National Institutes of Health under Grant CA 54896. The work of M. A. Lubinski was supported under a National Science Foundation Graduate Research Fellowship.

A. R. Skovoroda is with the Institute of Mathematical Problems of Biology, Russian Academy of Sciences, Pushchino, Russia 142292.

S. Y. Emelianov, M. A. Lubinski, and M. O'Donnell are the Electrical Engineering and Computer Science Department and the Bioengineering Program, University of Michigan, Ann Arbor, MI 48109 USA.

A. P. Sarvazyan is with the Institute of Theoretical and Experimental Biophysics, Russian Academy of Sciences, Pushchino, Russia 142292.

IEEE Log Number 9400143.

II. Theory

A theoretical model for the forward elastic problem formulated here as a boundary value problem with applied surface displacements was used to predict internal phantom displacements and strains. Not only will this model help assess the accuracy of strain images, it will facilitate both algorithm development for elasticity reconstruction and optimization of applied external surface deformations.

The parameters describing the deformation of an elastic or viscoelastic body, i.e., spatial distribution of displacements, strain and stress, must satisfy the equations of continuum mechanics presented below [21], [25], [26].

The most general form of Newton's 2nd law describing the motion of a mechanical body is

$$\sum_{j=1}^{3} \frac{\partial \sigma_{ij}}{\partial x_j} + f_i = \rho \frac{\partial^2 u_i}{\partial t^2} \quad i = 1, 2, 3, \tag{1}$$

where σ_{ij} is one component of the 2nd ranked stress tensor, u_i is the displacement in the x_i direction, f_i is the body force per unit volume acting on the body in the x_i direction, t is time and ρ is density. Equation (1) must be satisfied at every internal point of the body.

Assuming linear elasticity, the components of the stress tensor in an isotropic, continuous compressible medium including viscosity are:

$$\sigma_{ij} = \lambda \Theta \delta_{ij} + 2\mu \varepsilon_{ij} + \xi \frac{\partial \Theta}{\partial t} \delta_{ij} + 2\eta \frac{\partial \varepsilon_{ij}}{\partial t}, \tag{2}$$

where

$$\Theta = \nabla \cdot \mathbf{u} = \varepsilon_{11} + \varepsilon_{22} + \varepsilon_{33} \tag{3}$$

is the trace of the strain tensor, δ_{ij} is the Kronecker delta symbol and ε_{ij} is one component of the 2nd ranked symmetric strain tensor, defined as

$$\varepsilon_{ij} = \frac{1}{2}\left(\frac{\partial u_i}{\partial x_j} + \frac{\partial u_j}{\partial x_i}\right). \tag{4}$$

In (2) the first two terms describe the elastic behavior and the last two terms the damping of the mechanical body. The parameters λ and μ are the Lame coefficients and parameters ξ and η are the coefficients of viscosity. Therefore, in general, any isotropic continuous mechanical body can be characterized by a **spatial distribution** of the viscoelastic parameters, such as λ, μ, ξ and η. This model of a continuous mechanical body applies for soft tissue at a spatial scale sampled by diagnostic ultrasound (i.e., at a scale greater than or comparable to an ultrasound wavelength). Note that some tissues, such as muscle, are anisotropic [21], necessitating a more general stress-strain relationship than (2) [25], [26]. Anisotropic materials are not considered in this paper.

Although the elastic component of the stress-strain relation is written in terms of the Lame coefficients in (2), other more common elastic moduli can be derived from these two fundamental parameters. For example, the well-known bulk modulus B is simply defined as $B = \lambda + (2/3)\mu$ and the shear modulus is simply μ. Expressions for other common parameters, such as Young's modulus E and Poisson's ratio ν, can be written in terms of the Lame coefficients:

$$\nu = \frac{\lambda}{2(\lambda + \mu)}$$
$$E = \mu \frac{3\lambda + 2\mu}{(\lambda + \mu)}.$$

If the body is deformed very slowly to the final position, only static deformation need be considered. For static deformation (1) reduces to:

$$\sum_{j=1}^{3} \frac{\partial \sigma_{ij}}{\partial x_j} + f_i = 0 \quad i = 1, 2, 3. \tag{5}$$

Similarly, all time dependent terms in the stress-strain relation vanish so that the components of the stress tensor become

$$\sigma_{ij} = \lambda \Theta \delta_{ij} + 2\mu \varepsilon_{ij}. \tag{6}$$

That is, for static deformation a mechanical body will act solely as an elastic body, completely characterized by two parameters λ and μ.

The general expressions of linear elasticity can be greatly simplified by assuming that all soft tissues, and tissue-like materials, are incompressible (i.e., Poisson's ratio equals 0.5). Since the Poisson's ratio approaches 0.5 for most soft tissue [27], the assumption of incompressibility is valid. If the mechanical body is incompressible, then

$$\Theta = \nabla \cdot \mathbf{u} = 0, \tag{7}$$

which determines the volume change due to deformation. Similarly, if the material volume does not change, then the longitudinal Lame constant λ approaches infinity. Under these conditions, the stress-strain relation (6) for static deformation reduces to

$$\sigma_{ij} = p\delta_{ij} + 2\mu \varepsilon_{ij}, \tag{8}$$

where p is the static internal pressure, defined as [28]

$$\lim_{\frac{\lambda}{\mu} \to \infty, \theta \to 0} (\lambda \theta) = p.$$

Therefore, deformation of an incompressible medium can be completely characterized by a single material parameter μ (or $E = 3\mu$, as illustrated in Fig. 1 where μ/E is plotted as a function of Poisson's ratio). That is, the shear (or Young's) modulus completely describes the static elastic properties of soft tissue, where its value may vary widely between different types of soft tissue.

Finally, a closed set of coupled differential equations for unknown displacement vector components $u_i(x_1, x_2, x_3)$ and pressure $p(x_1, x_2, x_3)$ describing static deformation of a viscoelastic, incompressible material can be generated by combining (3)–(5), (7), (8) and eliminating σ_{ij} and ε_{ij}:

$$\partial \frac{\partial p}{x_1} + 2\frac{\partial}{\partial x_1}\left(\mu \frac{\partial u_1}{\partial x_1}\right) + \frac{\partial}{\partial x_2}\left(\mu\left(\frac{\partial u_1}{\partial x_2} + \frac{\partial u_2}{\partial x_1}\right)\right) + \frac{\partial}{\partial x_3}\left(\mu\left(\frac{\partial u_1}{\partial x_3} + \frac{\partial u_3}{\partial x_1}\right)\right) + f_1 = 0$$

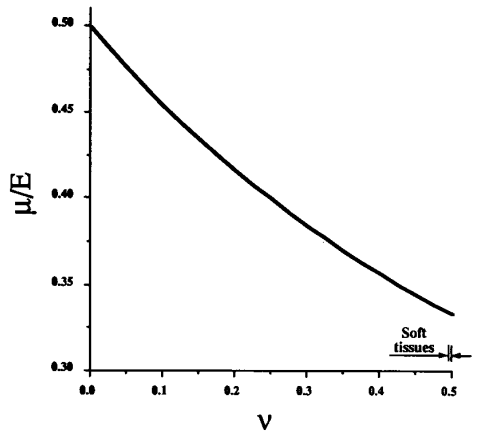

Fig. 1. The ratio of shear modulus to Young's modulus (μ/E) is plotted as a function of Poisson's ratio (ν). Note that the region of Poisson's ratio for soft tissue is shown, where the ratio of moduli approaches 1/3.

$$\begin{aligned}
&\partial\frac{\partial p}{x_2}+2\frac{\partial}{\partial x_2}\left(\mu\frac{\partial u_2}{\partial x_2}\right)+\frac{\partial}{\partial x_1}\left(\mu\left(\frac{\partial u_1}{\partial x_2}+\frac{\partial u_2}{\partial x_1}\right)\right)\\
&\quad+\frac{\partial}{\partial x_3}\left(\mu\left(\frac{\partial u_2}{\partial x_3}+\frac{\partial u_3}{\partial x_2}\right)\right)+f_2=0\\
&\frac{\partial p}{\partial x_3}+2\frac{\partial}{\partial x_3}\left(\mu\frac{\partial u_3}{\partial x_3}\right)+\frac{\partial}{\partial x_1}\left(\mu\left(\frac{\partial u_1}{\partial x_3}+\frac{\partial u_3}{\partial x_1}\right)\right)\\
&\quad+\frac{\partial}{\partial x_2}\left(\mu\left(\frac{\partial u_2}{\partial x_3}+\frac{\partial u_3}{\partial x_2}\right)\right)+f_3=0\\
&\frac{\partial u_1}{\partial x_1}+\frac{\partial u_2}{\partial x_2}+\frac{\partial u_3}{\partial x_3}=0.
\end{aligned}\tag{9}$$

The first three equations are the equations of equilibrium for a mechanical body written in terms of the displacements, and the last equation is the condition of incompressibility. Note that any spatial variations in elasticity $\mu(x_1,x_2,x_3)$ are explicitly included in (9).

The system of (9) has an infinite number of solutions, where the unique solution is determined by the boundary conditions. The general statement of mechanical boundary conditions is:

$$\left(\sum_j \sigma_{ij}n_j - F_i\right)\delta\left(u_i-u_i^0\right)=0,\quad i=1,2,3,\tag{10}$$

where n_j is the jth component of the unit normal vector at the body surface, F_i is the force per unit area at the surface acting in direction x_i and δ is a symbol of variation [26]. In general, the boundary conditions can be split, where external applied forces are specified for part of the boundary and displacements for other parts. For any given external force F_i applied to some part of the surface, the corresponding equation in (10) is satisfied by the first term with no restriction on the u_i component of the surface displacement. In contrast, if the displacement u_i^0 is given, the corresponding equation is satisfied by the second term with no additional restriction on the stress tensor. By solving the system of (9) with corresponding boundary conditions, the displacement field can be obtained and, therefore, components of the strain tensor can be simply calculated from (4). Note that the stress components in the boundary conditions (10) can be written in terms of the displacements and pressure using (4) and (8).

The main goal of elasticity imaging is to reconstruct the elastic modulus of any desired internal part of tissue. Based on the above analysis for incompressible media, elasticity imaging is reduced to reconstruction of the spatial distribution of the Young's modulus $E(x_1,x_2,x_3)$ (or $\mu(x_1,x_2,x_3)$). After elimination of the unknown pressure $p(x_1,x_2,x_3)$, (9) can be used to reconstruct the distribution of elasticity [29]. It is important to note that it is not necessary to know the boundary conditions in detail. Moreover, all information needed for elasticity reconstruction comes from the region of interest. This approach, however, requires knowledge of the spatial distribution of all components of the strain tensor in the region of interest. Practical implementation, therefore, is limited by difficulties in measuring all components of the displacement vector [24], [30]. As a result, different simplified approaches have been proposed in the static regime [16], [19], [29], [31], [32], and in the dynamic regime [13], [20], [22], [23]. The utility of these simplified approaches is ultimately limited by their accuracy in describing experimental displacement and strain data for a general spatial distribution of Young's modulus.

Any simplified model uses a reduced set of parameters to characterize the elasticity distribution. Limited experimental information is then used to solve for these model parameters. For example, if a solid tumor is modeled as a homogeneous, spherical inclusion, then we must only estimate the Young's modulus, diameter and location of this sphere. Solution of the forward elastic problem using a particular mechanical model of tissue can be compared to measured displacement and/or strain fields. This process can be computed iteratively, where model parameters are adjusted on each iteration to maximize the correlation between measurements and predictions. Note that this process will converge to the unique solution only if there is a monotonic relation between model parameters and the limited experimental data. The accuracy of the elasticity distribution obtained in this way, therefore, is directly related to the appropriateness of the simplified model used to describe the actual distribution of inhomogeneities. In general, an appropriate model must be used or elasticity reconstruction will exhibit significant artifacts.

To illustrate some of the difficulties in elasticity reconstruction, two simple examples will be given. An analytic solution for compressible, uniformly deformed bodies having spherical or cylindrical inclusions inside has been derived by Goodier [33]. For a cylindrical inclusion, the inclusion's longitudinal axis is perpendicular to the direction of applied deformation. Similar solutions for an incompressible medium can be readily derived from Goodier's results as the value of the Poisson's ratio ν approaches 0.5. Based on this analysis, the normalized longitudinal strain component ε in the direction of the applied deformation within the inclusion is shown in Fig. 2 for a cylindrical inclusion (2-D) and a spherical inclusion (3-D) as functions of the relative Young's modulus of the inclusion (E/E_0). Also presented in this figure is the result for a layered inclusion (1-D). For all cases, ε_0 represents the corresponding strain component in the homogeneous body having Young's

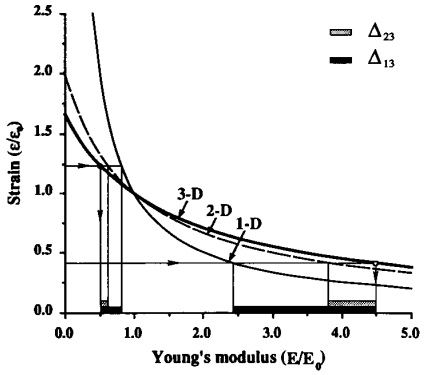

Fig. 2. Relative strain in the direction of the applied deformation calculated inside an inclusion as a function of the relative Young's modulus of inclusion.

modulus E_0. Using these functional relations, the unknown Young's modulus of an inclusion can be reconstructed based on the measured value of ε. For example, from the experimental value of ε inside the spherical inclusion, the Young's modulus of that inclusion can be estimated, as illustrated in Fig. 2. In general, however, such simple interpretation of experimental data is impossible, and moreover, may lead to significant errors in estimating the Young's modulus. For example, errors in interpreting measurements from a spherical inclusion using 2- and 1-D models, noted as Δ_{23} and Δ_{13}, are also shown in Fig. 2. Clearly, significant error can occur if the particular mechanical model of tissue is inappropriate.

Another example further illustrates the importance of using an appropriate particular model to describe the mechanical properties of tissue abnormalities. Consider a more complex spatial distribution of the Young's modulus. Assume that $E(x_1, x_2, x_3) = E(r)$, where the center of the spherical (r, θ, ϕ) or cylindrical (r, θ) system of coordinates is placed at the center of a spherically symmetric (3-D) or cylindrically symmetric (2-D) inhomogeneity such that the direction $\theta = 0$ is parallel to the direction of an applied deformation. Based on Goodier's solution, we attempt to find the solutions of (9) for 3-D in the form

$$\begin{aligned} u_r &= \frac{1}{4}U(r)(1 + 3\cos(2\theta)) \\ u_\theta &= V(r)\sin(2\theta) \\ u_\phi &= 0 \\ p &= P_0(r) + P_1(r)\cos(2\theta), \end{aligned} \tag{11a}$$

and for 2-D in the form

$$\begin{aligned} u_r &= U(r)\cos(2\theta) \\ u_\theta &= V(r)\sin(2\theta) \\ p &= P_1(r)\cos(2\theta). \end{aligned} \tag{11b}$$

Using the incompressibility condition, we find that

$$\begin{aligned} V &= -\frac{1}{4}\left(2U + r\frac{\partial U}{\partial r}\right) \quad \text{for 3-D,} \\ V &= -\frac{1}{2}\left(U + r\frac{\partial U}{\partial r}\right) \quad \text{for 2-D.} \end{aligned} \tag{12}$$

Substituting expressions (11) and (12) into either the spherical or cylindrical form of (9) and eliminating the pressure, for both 2- and 3-D cases we obtain an equation coupling $U(r)$ and $E(r)$:

$$r^4\frac{\partial^4 U}{\partial r^4} + a_3 r^3\frac{\partial^3 U}{\partial r^3} + a_2 r^2\frac{\partial^2 U}{\partial r^2} + a_1 r\frac{\partial U}{\partial r} + a_0 U = 0, \tag{13}$$

with

$$\begin{aligned} a_3 &= 2(4 + \gamma r), \\ a_2 &= r(r\Gamma + 10\gamma), \\ a_1 &= 2(r^2\Gamma - 3\gamma r - 12), \\ a_0 &= 4(r^2\Gamma + 6) \text{ for 3-D,} \end{aligned}$$

and

$$\begin{aligned} a_3 &= 2(3 + \gamma r), \\ a_2 &= r^2\Gamma + 7\gamma r - 3, \\ a_1 &= r^2\Gamma - 7\gamma r - 9, \\ a_0 &= 3(r^2\Gamma + \gamma r + 3) \text{ for 2-D,} \end{aligned}$$

where

$$\gamma = \frac{1}{E}\frac{\partial E}{\partial r}, \quad \Gamma = \frac{1}{E}\frac{\partial^2 E}{\partial r^2}.$$

In the particular case where $E = E_0 =$ constant, the coefficients a_i are constants and the general solution of (13) for the unknown function $U(r)$ can be found analytically [33]. For a general function $E = E(r)$, the solution of (13) can be found numerically. The boundary conditions $U(0) = 0$ and

$$\lim_{r\to\infty}\left[\frac{U(r)}{r}\right] \to \varepsilon_0,$$

must be satisfied. In addition, all components of the displacement and both the radial longitudinal σ_{rr} and shear $\sigma_{r\theta}$ components of the stress tensor must be continuous [26]. For example, using $E = E(r)$ shown in Fig. 3(a), the radial component ε_{rr} of the strain tensor can be computed along the axis $\theta = 0$, as presented in Fig. 3(b). This Young's modulus distribution corresponds to a complex inhomogeneity having relatively soft interior and hard exterior surrounded by material having Young's modulus E_0. The position of $E(r)$'s maximum is defined as r_0 and again, the normalizing value ε_0 is the corresponding strain component in the homogeneous body.

Reconstruction of the elasticity distribution for this case is more complicated than in the previous example, requiring at least measurements of the displacement $U(r)$ along the axis $\theta = 0$ with solution of (13) for an unknown distribution $E = E(r)$ under the conditions $E = E_0$ and $\frac{\partial E}{\partial r} = 0$ for any value r outside the inhomogeneity. Note that quantitative differences between model results presented in Fig. 3(b) show the need for accurate interpretation of experiments since model mismatch (i.e., sphere, cylinder, "layers") may lead to significant errors in reconstruction.

Additionally, not only are proper dimensional considerations important, but the type of deformation is critical in interpreting strain measurements. The two examples presented above assume uniform external deformation of the body. This simple assumption will rarely be the case in practice, especially for

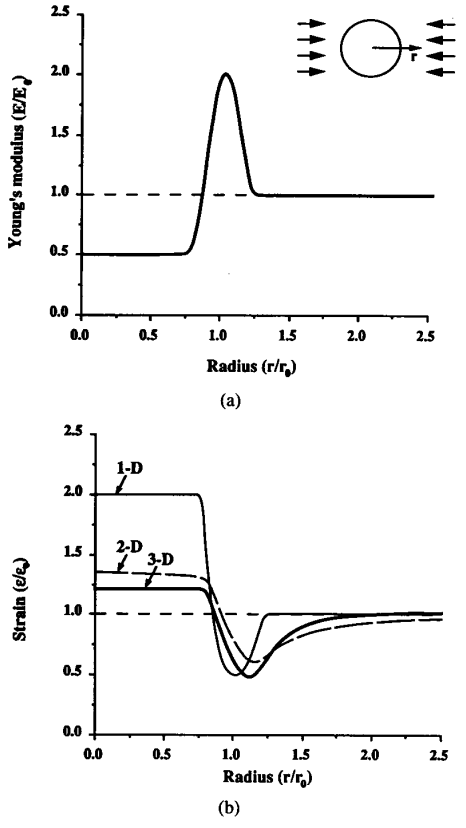

Fig. 3. (a) Young's modulus and (b) the corresponding relative radial strain components, calculated for a inhomogeneity in 3-, 2-, and 1-D statements, as functions of the normalized radial coordinate.

real clinical applications. Consequently, a realistic, nonuniform deformation due to complex, mixed boundary conditions must be properly considered if strain measurements are to be used for reconstruction of the elasticity distribution.

As shown above, experimental displacement and strain fields must be used with an appropriate model for proper reconstruction of the elasticity distribution. Therefore, it is important to test the agreement between experimental data and predictions of the forward problem computed with the same model that ultimately will be used for reconstruction. In the next section, experimental results obtained with the newly developed speckle tracking algorithm described in a companion paper [24] are compared with theoretical predictions based on the numerical solution of (9) when the boundary conditions are taken into account. As a first step, only 2-D problems are investigated in the remainder of this paper.

III. 2-D Model

Preliminary experiments were performed on a number of gel-based phantoms including a particular pair used for all results reported here. All phantoms were designed to qualitatively simulate the mechanical properties of soft tissue [12], [13], [16], [19]. Originally, two homogeneous cylindrical gels were made at the same time with nearly identical mechanical characteristics [1]. Each 88 mm diameter by 140 mm long cylinder was constructed from 5.5% by weight gelatin (Knox Gelatine, Inc., Englewood Cliffs, NJ). A circular longitudinal hole was made in the center of one phantom and filled with 12% by weight gelatin to simulate a hard inclusion 32 mm in diameter. The presence of the inclusion in the second phantom could not be detected by manual palpation. In both the homogeneous phantom and the phantom with central hard inclusion, 0.4% by weight polystyrene microspheres (Analytical Grade Cation Exchange Resin, AG 50 W-X12, Bio-RAD Laboratories, Hercules, CA) with a diameter of 40–120 μm were added as ultrasonic scattering centers. The concentration of microspheres in the inclusion was the same as in surrounding material making both phantoms approximately identical in scattering characteristics.

A schematic of the experimental system used in the present study is presented in Fig. 4. The phantom was placed in the tank so that its cylindrical axis was perpendicular to the axis of a 128 channel, 1-D transducer array operating at 3.5 MHz. This transducer was attached to the bottom of the tank. The phantom was centered in the tank so that the image plane approximated the central plane perpendicular to the longitudinal axis of the phantom. The tank was filled with water to provide contact between the array and phantom. A set of seven hydraulically driven pistons was positioned so that different surface displacements could be applied to the top half of the phantom. Pistons were 14 mm wide by 150 mm long rectangular blocks supported by a circular arc. The center of this support was located on the central longitudinal axis of the phantom such that any piston's force (displacement) initially was radially directed to the phantom's surface. Every piston could be operated independently to produce any desired distribution of surface displacement. The surface of every piston, as well as the bottom surface of the tank, was made rough to prevent slippage between that surface and the phantom during deformation. Also, the transducer surface was a rubberlike material preventing slippage.

The experimental system of Fig. 4 can produce varied strain patterns inside the object to test different inversion algorithms. In the experiments presented here, however, surface displacements were produced only by the vertical piston located at the top of the phantom. Displacement of this piston was controlled by measuring arrival time differences to the central element of the array. Future studies will investigate displacement and strain fields produced by alternate surface displacement.

Internal displacement of the phantom was estimated using the procedure of [24], [34]. Complex baseband images were generated with a synthetic aperture approach, where special processing was included in image reconstruction to minimize grating lobes produced by the large array elements (approximately 1.5 acoustic wavelengths). Because traditional speckle tracking techniques fail in the limit of very large motion (compared to an acoustic wavelength), the method of [24] accumulates displacement over a large set of small, differential displacements. Experimental results presented below used a set of 21 images over a total vertical piston displacement of 4 mm (i.e., 200 μm steps) to quantitatively estimate the vertical longitudinal component (ε_{22}) of the strain tensor.

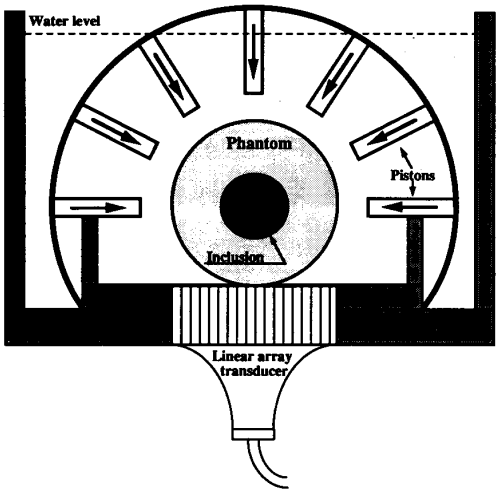

Fig. 4. Schematic representation of the experimental system and phantom geometry. The bottom of the cylindrical phantom, 88 mm in diameter and 150 mm long, contacts a 128 element linear transducer array used to image the cross-sectional central plane. A set of the pistons providing the deformation is on the top, where only the central piston was displaced by 4 mm in the present experiment.

Based on the particular geometry of our experimental system and phantoms, the theoretical model can be simplified. Because the phantom is placed in the tank so that the image plane approximates the central axial plane ($x_3 = 0$) of the phantom, a 2-D approximation of (9) can be used. This assumes that out-of-plane motion in the imaging plane is relatively small compared to in-plane displacements, and that in-plane displacements do not vary as a function of the axial coordinate in the region close to the imaging plane [26]. Indeed, the x_3-symmetry of the phantom and x_3-symmetry of the boundary conditions directly leads to the condition that $u_3(x_1, x_2, 0) = 0$. In a region close to the plane $x_3 = 0$, a Taylor series expansion of the displacement components and pressure can be incorporated into (9), assuming no slippage for the points connected to the piston or the bottom of the tank, to evaluate the x_3 dependence of these parameters. Such an analysis shows that a 2-D approximation is accurate over the extent of the imaging plane.

With these assumptions, (9) reduces to:

$$\begin{aligned}
&\frac{\partial p}{\partial x_1} + 2\frac{\partial}{\partial x_1}\left(\mu\frac{\partial u_1}{\partial x_1}\right) + \frac{\partial}{\partial x_2}\left(\mu\left(\frac{\partial u_1}{\partial x_2} + \frac{\partial u_2}{\partial x_1}\right)\right) = 0 \\
&\frac{\partial p}{\partial x_2} + 2\frac{\partial}{\partial x_2}\left(\mu\frac{\partial u_2}{\partial x_2}\right) + \frac{\partial}{\partial x_1}\left(\mu\left(\frac{\partial u_1}{\partial x_2} + \frac{\partial u_2}{\partial x_1}\right)\right) + f_2 = 0 \\
&\frac{\partial u_1}{\partial x_1} + \frac{\partial u_2}{\partial x_2} = 0,
\end{aligned} \tag{14}$$

where only the f_2 component of the force per unit volume, acting in the x_2 direction, does not vanish for our experimental configuration. This vertical component of the volume force is the simple combination of gravity and buoyancy, defined as

$$f_2 = g(\rho - \rho_0),$$

where g is the gravitational acceleration and ρ and ρ_0 are the density of the phantom and the water, respectively.

To analyze deformations of a phantom, therefore, the system of partial differential equations (14) with proper boundary conditions has to be solved. Because an analytic expression of the solution cannot be obtained, numerical methods must be used. The algorithm employed in this paper is a finite difference method. To properly model both bounded inclusions and inhomogeneities having continuous spatial distribution of Young's modulus, an integro-interpolative method has been used to construct the conservative finite differential scheme with a second order approximation to spatial derivatives [35]. In addition, the iterative algorithm used here is based on a stabilization method commonly employed in the numerical solution of such partial differential equations [35]. This method assumes that the unknowns u_1, u_2 and p are not only functions of spatial coordinates, but also depend on an additional dummy variable τ, i.e.,

$$\begin{aligned}
u_1 &= u_1(x_1, x_2, \tau) \\
u_2 &= u_2(x_1, x_2, \tau) \\
p &= p(x_1, x_2, \tau).
\end{aligned} \tag{15}$$

With this assumption, we can write a new system of equations, where the right hand side is now simply the first derivative with respect to the dummy variable:

$$\begin{aligned}
&\frac{\partial p}{\partial x_1} + 2\frac{\partial}{\partial x_1}\left(\mu\frac{\partial u_1}{\partial x_1}\right) + \frac{\partial}{\partial x_2}\left(\mu\left(\frac{\partial u_1}{\partial x_2} + \frac{\partial u_2}{\partial x_1}\right)\right) = \frac{\partial u_1}{\partial \tau} \\
&\frac{\partial p}{\partial x_2} + 2\frac{\partial}{\partial x_2}\left(\mu\frac{\partial u_2}{\partial x_2}\right) + \frac{\partial}{\partial x_1}\left(\mu\left(\frac{\partial u_1}{\partial x_2} + \frac{\partial u_2}{\partial x_1}\right)\right) + f_2 = \frac{\partial u_2}{\partial \tau} \\
&\frac{\partial u_1}{\partial x_1} + \frac{\partial u_2}{\partial x_2} = k\frac{\partial p}{\partial \tau},
\end{aligned} \tag{16}$$

where k is a normalized coefficient. Note that the boundary conditions (10) will not change with assumption (15). The solution of (16) with boundary conditions (10), where the boundary conditions do not depend on the dummy variable τ, also is a solution of (14) in the limit that τ approaches infinity. In this limit, the right hand sides of (16) all vanish.

For the experimental system discussed above, there is another complication in specifying the boundary conditions. As shown in Fig. 5, the boundary conditions on the phantom are functions of the deformation, where the size of the contact regions to the bottom of the tank and the piston depend on the magnitude of the top surface displacement. Thus, the boundary conditions cannot be predicted *a priori* and must also be calculated.

Three main parts of the boundary are shown in Fig. 5(a) for the initial conditions of the phantom. At the bottom point, shown by an arrow, absence of any displacement was assumed, i.e., all components of the displacement vector are always equal to zero guaranteeing no net motion of the phantom. At the top point, also shown by an arrow in Fig. 5(a), only the u_1 component of the displacement vector is zero, which protects against any rotation of the phantom as a whole body and also insures that the vertical component u_2 of the displacement vector of this point is the same as the vertical displacement of the central piston. Therefore, at these two particular points displacements on the surface are defined. For all other points on the surface of the phantom, no forces are applied.

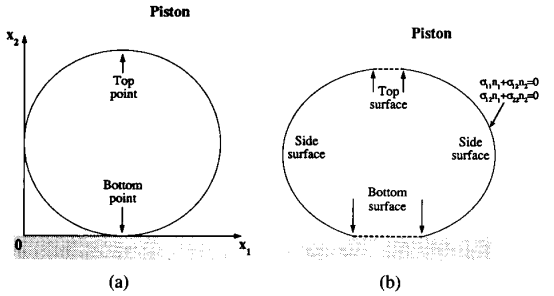

Fig. 5. Differences in boundary conditions on the phantom surface are shown, where (a) the central piston just contacts the surface of the phantom, (b) the central piston displaces the phantom surface.

In the deformed state [Fig. 5(b)] more than these two surface points are connected to the piston and the bottom of the tank. An iterative step-wise algorithm has been used to satisfy all boundary conditions as a function of the deformation. During each step of this process, every point on the phantom surface was tested for contact with either the piston (top half of the phantom surface) or the bottom of the tank (bottom half of the phantom surface). If a point was connected with the bottom at a particular step, no more motion of this point was allowed at subsequent steps. Similarly, if a point contacted the piston at a particular step, the displacement of this point was restricted to vertical motion equal to the displacement of the piston in all subsequent steps. For all other boundary points not connected with either the piston or the bottom of the tank, the absence of any external force was assumed. Therefore, the boundary conditions for these points were satisfied by the first term in (10) with $F_i = 0$:

$$\sigma_{11}n_1 + \sigma_{12}n_2 = 0$$
$$\sigma_{12}n_1 + \sigma_{22}n_2 = 0,$$

where n_1 and n_2 are the components of the unit normal vector at the phantom surface. These equations were written in terms of the displacement components and pressure using (4) and (8) and a one-sided, second-order finite difference approximation to the spatial derivatives. In addition, every point connected to the bottom of the tank or to the piston on the previous iteration was tested for continued connection since contact may result solely from finite error in the iterative scheme.

By replacing the differential equations with finite differences, the mechanical properties of the body must be properly discretized on a spatial grid with sampling fine enough to capture all variations in the Young's modulus. A proper grid is chosen so that any further decrease in the grid itself does not result in significant changes in the computed displacement and strain fields. In this study, a uniform, Cartesian discretization of 1.5 mm was used for the 88 mm diameter, cylindrical phantom. The appropriateness of this spacing for these particular phantoms is illustrated in the next section. In the numerical scheme, iterations were continued until the mean squared value of the relative error for displacements and pressure was less than 10^{-6}.

To more closely match the true mechanical properties of the inhomogeneous phantom, the hard inclusion was simulated with two layers, a core having 2.5 times larger Young's modulus than the surrounding material and an outer annulus surrounding the core with a Young's modulus only 1.75 times greater than the surrounding material. The diameter of the core was assumed to be 28 mm and the thickness of the annulus 2 mm, resulting in a total inclusion diameter of 32 mm. This assumption is based on the procedure for making the inclusion, where the hole in the phantom is filled with a gelatin solution at a temperature slightly higher than that of the phantom. The temperature difference can produce the small annulus between the inclusion and the surrounding material. It is assumed that the Young's modulus of this region should be between that of the phantom itself and the inclusion. The value of the relative Young's modulus for the inclusion's core was chosen based on an approximately linear dependence of the Young's modulus on gel concentration in this range [1].

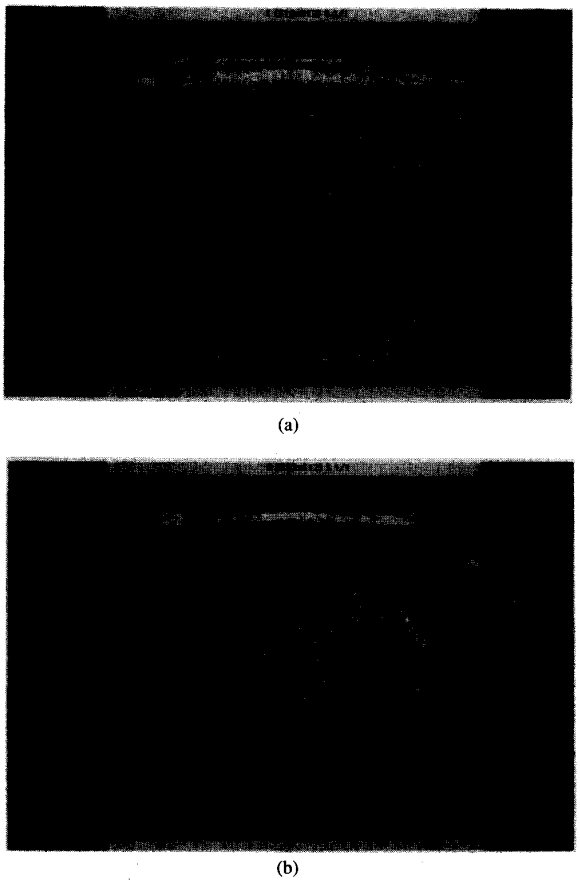

Fig. 6. Conventional B-scan images of (a) homogeneous phantom, shown in the final deformed position and (b) phantom with central hard inclusion, shown in the initial undeformed position.

IV. Results

In Fig. 6, B-scan images are presented for both the homogeneous phantom and the phantom with hard inclusion. The images are displayed over a 100 × 100 mm area, where the transducer array is at the bottom and the central piston is located at the top. Fig. 6(a) corresponds to the homogeneous phantom, displayed after the top piston is displaced vertically

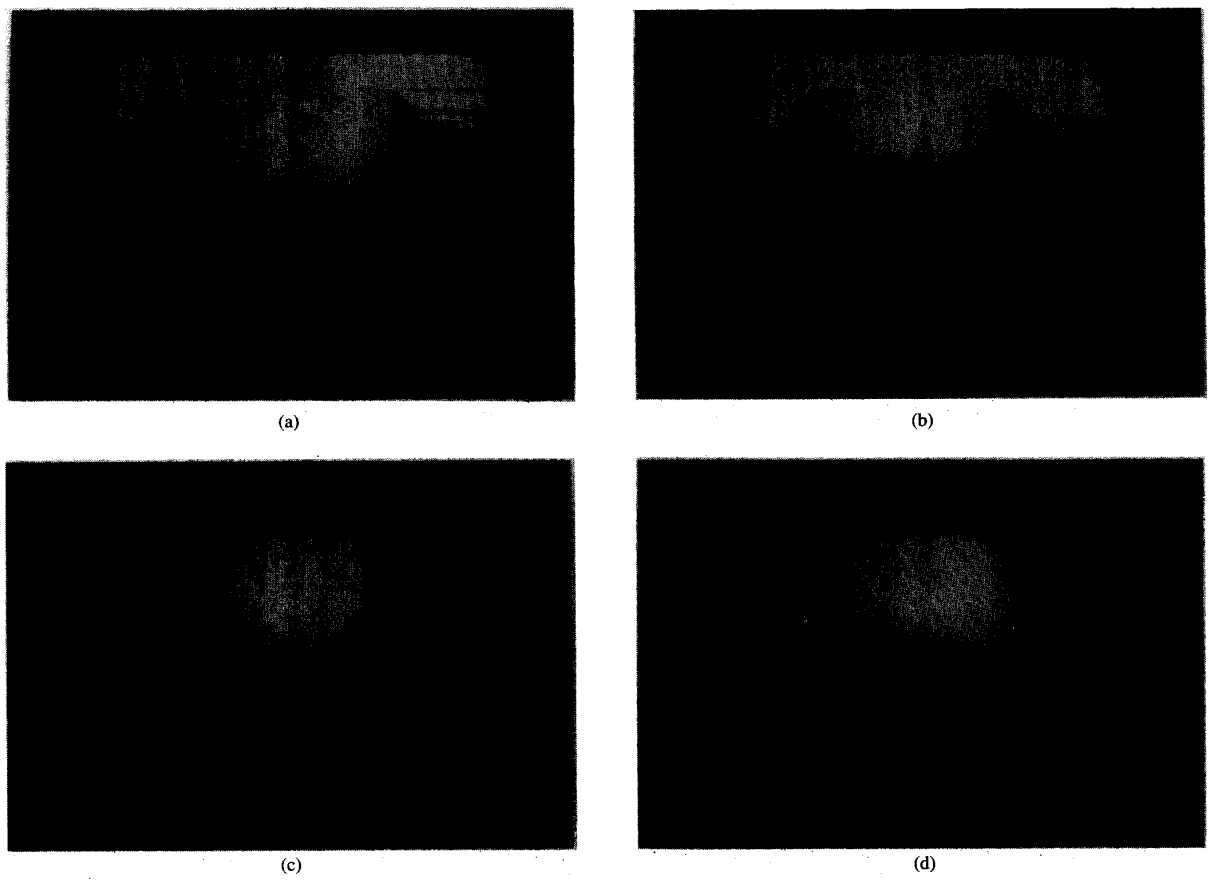

Fig. 7. Measured displacement images of (a) homogeneous phantom and (b) phantom with hard inclusion are compared to theoretical prediction of the displacement for the same (c) homogeneous and (d) inhomogeneous phantoms. All images use the same absolute display dynamic range, where white represents 4 mm vertical displacement and black represents no displacement.

by 4 mm. In contrast, Fig. 6(b) shows the phantom with hard inclusion in the initial undeformed position. It is hard to detect the inclusion from the B-scans. Although not of the highest quality because a synthetic aperture reconstruction was used, these images are sufficient for displacement and strain measurements as described in [24].

The corresponding vertical displacement distributions created by the central vertical piston are shown in Fig. 7, where the two top panels [Fig. 7(a) and (b)] are measured values of the displacement and the two bottom panels [Fig. 7(c) and (d)] are simulated values. Left panels represent the homogeneous phantom and right panels the phantom with hard inclusion. All images cover an area of 100 × 100 mm, where the same quantitative gray scale is used for all images. Here full white represents a 4 mm negative displacement and full black corresponds to no displacement. The largest displacement magnitudes can be seen at the top of these images, where the piston provided the surface displacement, with smooth reduction to zero at the constrained bottom surface. Nonzero measured displacement outside the phantom is related to imaging artifacts and cannot be filtered. Nevertheless, the quality of displacement images within the phantom is sufficient for quantitative strain imaging.

Similar images of the ε_{22} strain component are presented in Fig. 8, where the strain field is displayed over the same 100 by 100 mm area. The signal-to-noise ratio of these images depends on position, but is estimated to be about 30 to 1 at the center of the inhomogeneous phantom [24]. Again, the left images are measured [Fig. 8(a)] and simulated [Fig. 8(c)] values of the strain component for the homogeneous phantom and the right panels show the same images [Fig. 8(b) and (d)] for the phantom with inclusion. Bright areas represent regions with the highest strain magnitude. In all images, the region of highest strain magnitude, starting at the top near the position of the piston and extending to the bottom where the transducer array has been attached, can be easily seen. Because the contact area of the phantom with the piston is not the same as that at the bottom of the tank, there is some difference in the strain distribution at the top and bottom of the phantom on both experimental and theoretical strain images. This effect also can be seen in Fig. 9. Note that all images in Fig. 8 are displayed over the same absolute dynamic range, i.e., over the same linear quantitative scale, where full brightness represents a longitudinal strain magnitude of 5.4% and larger, and complete darkness represents a strain magnitude of 2.7% and lower.

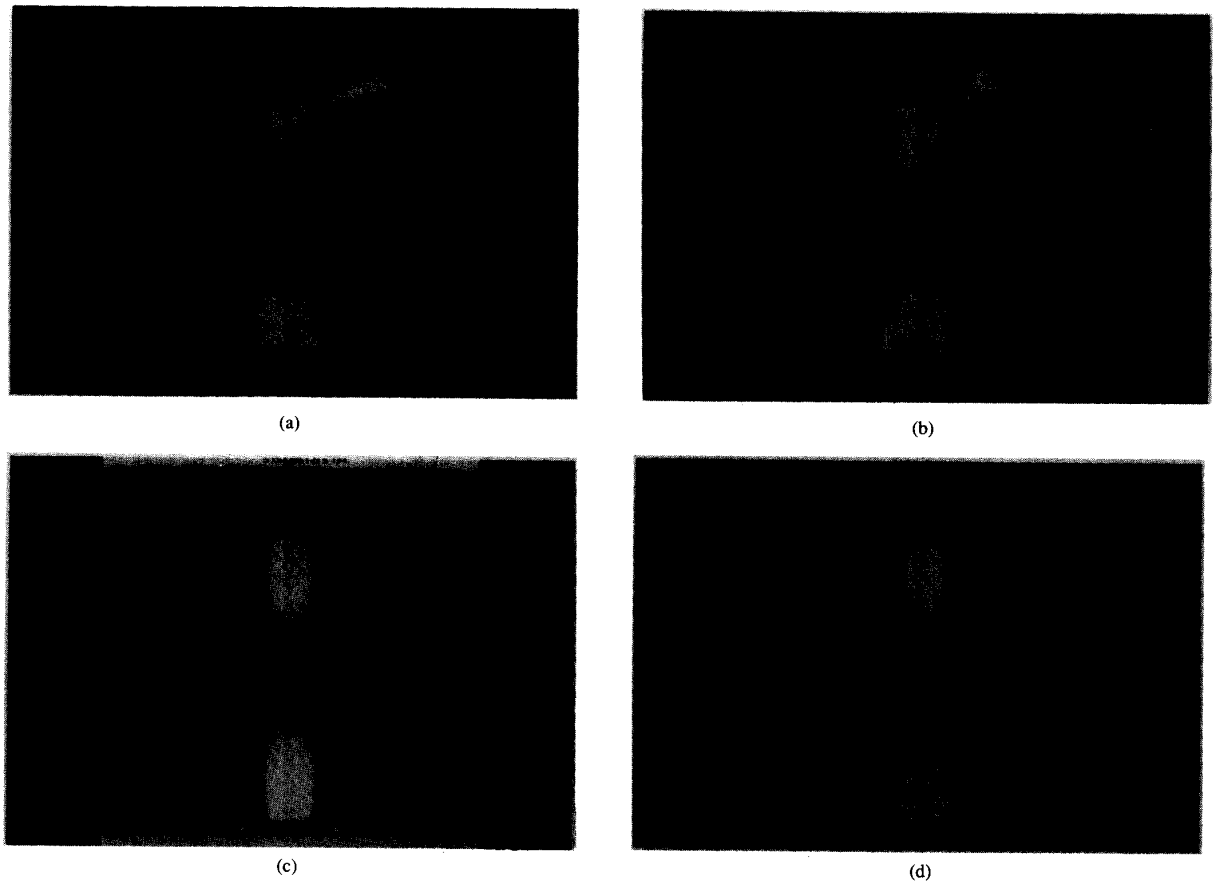

Fig. 8. Measured images of the vertical ε_{22} component of the strain tensor for the (a) homogeneous and (b) inhomogeneous phantoms are compared with model predictions for the same (c) homogeneous and (d) inhomogeneous phantoms. Note that all images are displayed over the same absolute dynamic range.

Strain A-scans for the different phantoms are compared in Fig. 9, where the top panel presents measured and predicted strain distributions along the central vertical line in the homogeneous phantom, and the bottom panel shows the same comparison for the phantom with inclusion. The results presented in Figs. 8 and 9 demonstrate that both qualitatively and quantitatively the theoretical predictions reasonably match measured strain images. Moreover, significant changes in the strain magnitude are clearly evident in the region of the inclusion. Differences between the true boundary conditions and the boundary conditions used in the model may cause the slight disagreement between theory and experiment evident in the bottom and top regions of the phantom. Finally, at the top of the phantom, where the mismatch in acoustic impedance between the piston and phantom is huge, the echo-signal was saturated and strain data were not computed.

V. Discussion

In this study a common linear elasticity model has been used to predict internal strains resulting from applied external displacements/forces [13], [16], [19], [21]–[23]. This model assumes an incompressible, linear elastic medium to formulate a boundary value problem. The method of finite differences was applied to obtain internal displacement/strain components for physical cases where the boundary conditions cannot be predicted *a priori*.

As reported in a companion paper, a newly developed method for accurate detection of tissue motion using phase sensitive speckle tracking has been applied to ultrasound elasticity imaging [24]. Preliminary studies show that quantitative strain images can be obtained with sufficient contrast-to-noise ratio to visualize small changes in elasticity. As is evident from Figs. 7–9, measured and simulated results match well with the exception of small regions close to the piston or bottom of the tank. This is probably caused by some boundary slippage during the measurements compared to the assumption of **no** boundary slippage in the computations. Nevertheless, the correlation presented in Figs. 7–9 shows that strain and displacement measurements are reasonably accurate suggesting that quantitative elasticity imaging for medical diagnosis, and other applications as well, is possible. Note that experimental results of the type presented here are sufficient to reconstruct the elasticity distribution for certain particular models of inhomogeneity [29], [31], [32]. If the

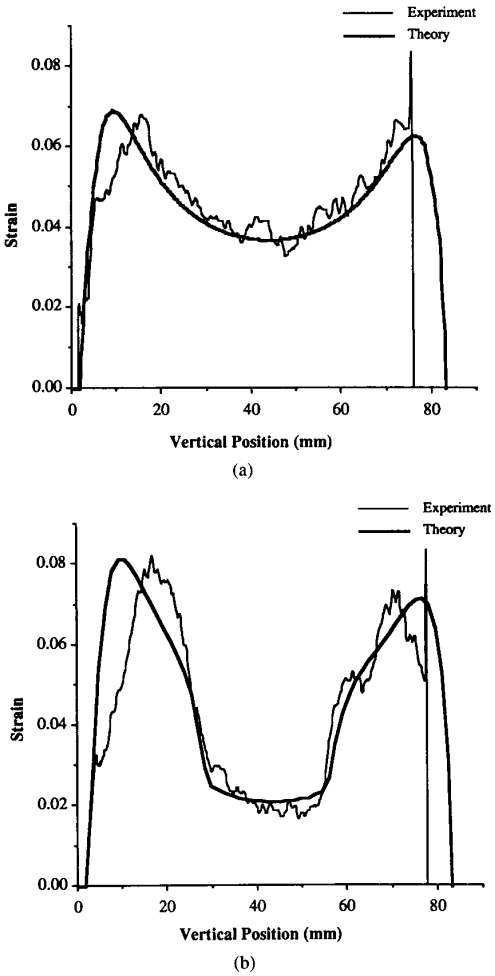

Fig. 9. Strain A-scans along the central vertical line for (a) homogeneous phantom and (b) phantom with inclusion. Note the strong correlation between theory and experiment.

lateral component of the displacement and associated strain components can be estimated [24], then restrictions on these particular models can be decreased.

For the experiments reported here, the applied deformation was about 5% of the initial size of the phantom, where the appropriateness of the linear model is not in question. At this level of average internal strain, a nonpalpable inclusion with Young's modulus only 2.5 times greater than surrounding material was easily detected. In clinical applications, e.g., breast imaging, much greater surface displacements can be applied potentially enhancing elasticity contrast resolution. In this regime, however, nonlinear elasticity theory must be used for proper interpretation of experimental data [21], [36]. Future studies will be directed toward analyzing strain measurements in the limit of large surface displacements and large average strains to identify the limit of the linear elastic model.

Simulation results shown in Figs. 7–9 were computed assuming the Young's modulus of the inclusion's core was 2.5 times larger than surrounding material. Much greater differences in elastic moduli are expected in real tissue. If similar results can be obtained in inhomogeneous, 3-D objects such as the female breast, then elasticity imaging may greatly expand the range of palpation for cancer detection. In general, however, elasticity inhomogeneities in the body can take on any geometric form at different locations. Different patterns of surface deformation may be needed to increase detectability of complex inhomogeneities especially if only limited strain data are measured. For example, the full piston array of Fig. 4 can be used with measurements of only the vertical, longitudinal component of the strain to expose inclusions far from the center of a cylindrical body. Consequently, to fully realize the potential of elasticity imaging, future work must be directed toward developing proper mathematical approaches based on different external deformations for detection of arbitrary lesions.

Quantitative strain and displacement results of the type presented here can be corrupted by tissue motion during the experiment. There are three primary sources of tissue motion in clinical imaging: cardiac induced motion, breathing and the finite propagation time of the deformation. The possible influence of these sources on strain images has already been discussed in the companion paper and must be studied in the future [24]. In conjunction with these experimental studies the approach used here can be modified to include these effects, where the motion/time dependence of the system will be considered explicitly in (1).

In conclusion, we have used a mechanical model considering the body as a linear elastic medium to predict internal displacement and strain images. Preliminary results show good agreement between measurement and theory even for the complex boundary conditions encountered in these studies. Such agreement suggests that quantitative reconstruction of the elastic modulus may be possible for complex objects such as the human body. Full reconstruction of the elastic properties of soft tissue without any assumptions about the spatial distribution of the elastic modulus should be based on reasonably good measurements of the complete 3-D spatial distribution of all strain tensor components. If limited measurements of the strain are obtained, then a correct simplified model of inhomogeneities must be used for reconstruction. The ultimate quality of reconstructions possible with a particular model based approach, therefore, is determined by the degree to which the particular model can accurately describe experimental data in complex objects.

ACKNOWLEDGMENT

General Electric, Acuson, and the College of Engineering of the University of Michigan are gratefully acknowledged.

REFERENCES

[1] A. P. Sarvazyan, V. I. Pasechnik, and S. E. Shnol, "Low speed of sound in gels and biological tissues," *Biofizika* , vol. 13, pp. 587–594, 1968.
[2] S. A. Goss, R. L. Johnston, and F. Dunn, "Comprehensive compilation of empirical ultrasonic properties of mammalian tissues," *J. Acoust. Soc. Amer.* , vol. 64, no. 2, pp. 423–457, 1978.
[3] T. A. Krouskop, D. R. Dougherty, and F. S. Levinson, "A pulsed Doppler ultrasonic system for making non-invasive measurements of

the mechanical properties of soft tissue," *J. Rehabil. Res. Dev.*, vol. 24, no. 2, pp. 1–8, 1987.
[4] R. Adler, J. M. Rubin, P. Bland, and P. Carson, "Characterization of transmitted motion in fetal lung: Quantitative analysis," *Med. Phys. 16*, pp. 333–337, 1988.
[5] L. Axel and L. Dougherty, "Heart wall motion: improved method of spatial modulation of magnetization for MR imaging," *Radiology* , vol. 169, pp. 59–63, 1988.
[6] R. M. Lerner, K. J. Parker, J. Holen, R. Gramiak, and R. C. Waag, "Sono-elasticity: Medical elasticity images derived from ultrasound signals in mechanically vibrated targets," *Acoust. Imaging* , vol. 16, pp. 317–327, 1988.
[7] M. Tristam, D. C. Barbosa, D. O. Cosgrove, J. C. Bamber, and C. R. Hill, "Application of Fourier analysis to clinical study of patterns of tissue motion," *Ultrasound in Med. & Biol. 14*, pp. 695–707, 1988.
[8] E. A. Zerhouni, D. M. Parish, W. J. Rogers, A. Yang, and E. P. Shapiro, "Human heart: tagging with MR imaging—a method for noninvasive assessment of mycardial motion," *Radiology*, vol. 169, pp. 164–172, 1988.
[9] M. Bertrand, J. Meunier, M. Doucet, and G. Ferland, "Ultrasonic biomechanical strain gauge based on speckle tracking," *Proc. 1989 IEEE Ultrason. Symp.*, pp. 859–864, 1989.
[10] J. Meunier and M. Bertrand, "Ultrasonic speckle motion inherent to tissue motion: theory and simulation," *Proc. 1989 IEEE Ultrason. Symp.* pp. 865–868, 1989.
[11] J. Meunier, et al., "Local myocardial deformation computed from speckle motion," *Computers in Cardiology*, pp. 133–136, 1989.
[12] R. M. Lerner, S. R. Huang and K. J. Parker, "'Sonoelasticity' images derived from ultrasound signals in mechanically vibrated tissues," *Ultrasound Med. Biol.* , vol. 16, no. 3, pp. 231–239, 1990.
[13] P. J. Parker, S. R. Huang, R. A. Musulin, and R. M. Lerner, "Tissue response to mechanical vibrations for "sonoelasticity imaging," *Ultrasound Med. Biol.*, vol. 16, no. 3, pp. 241–246, 1990.
[14] A. P. Sarvazyan and A. R. Skovoroda, "The new approaches in ultrasonic visualization of cancers and their qualitative mechanical characterization for the differential diagnostics," *Abstract of the All-Union Conference*, "The Actual Problems of the Cancer Ultrasonic Diagnostics, ' Moscow, November 1990.
[15] Y. Yamakoshi, J. Sato, and T. Sato, "Ultrasonic imaging of internal vibration of soft tissue under forced vibration," *IEEE Trans. Ultrason. Ferroelect. Freq. Contr.* , vol. 37, pp. 45–53, 1990.
[16] J. Ophir, I. Cespedes, H. Ponnekanti, Y. Yazdi, and X. Li., "Elastography: a quantitative method for imaging the elasticity of biological tissues," *Ultrasonic Imag. 13*, pp. 111–134, 1991.
[17] A. P. Sarvazyan and A. R. Skovoroda, "Tissue characterization in medical imaging in terms of viscoelastic mechanical properties," *Abstract of 6th World Congress in Ultrasound*, Copenhagen, September 1991.
[18] J. B. Fowlkes, S. Yemelyanov, J. G. Pipe, P. L. Carson , R. S. Adler, A. P. Sarvazyan, and A. R. Skovoroda, "Possibility of cancer detection by means of measurement of elastic properties," *Radiology*, vol. 185(P), pp. 206–207, 1992.
[19] H. Ponnekanti, J. Ophir, and I. Cespedes, "Axial stress distributions compressors in elastography: an analytical model," *Ultrasound Med. Biol.*, vol. 18, no. 8, pp. 667–673, 1992.
[20] A. Sarvazyan, A. Skovoroda, and D. Vucelic, "Utilization of surface acoustic waves and shear acoustic properties for imaging and tissue characterization," in *Acoustic Imaging, Ermert, H, Harjes, HP, (eds)*, v. 19, pp. 463–467, Plenum Press, New York (1992).
[21] Y. C. Fung, *Biomechanics. Mechanical properties of living tissues.* New York: Springer-Verlag, 1981.
[22] J. M. Pereira, J. M. Mansour, and B. R. Davis, "Analysis of shear wave propagation in skin; application to an experimental procedure," *J. Biomechanics* , vol. 23, no. 8, pp. 745–751, 1990.
[23] J. M. Pereira, J. M. Mansour, and B. R. Davis, "The effects of layer properties on shear disturbance propagation in skin," *J. Biomechanics Eng.*, vol. 113, pp. 30–35, 1991.
[24] M. O'Donnell, A. R. Skovoroda, B. M. Shapo, and S. Y. Emelianov, "Internal displacement and strain imaging using ultrasonic speckle tracking," submitted for publication in the *IEEE Trans. Ultrason. Ferroelect. Freq. Contr.*, this issue, pp. 314-325.
[25] L. D. Landau and E. M. Liftshitz, *Theory of elasticity.* Moscow: Nauka, 1965.
[26] Y. N. Rabotnov, *Mechanics of solid structures.* Moscow: Nauka, 1979.
[27] A. P. Sarvazyan, "Low frequency acoustic characteristics of biological tissues," *Mechanics of Polymers*, vol. 4, pp. 691–695, 1975.
[28] M. A. Biot, *Mechanics of Incremental Deformations.* New York: Wiley, 1965.
[29] A. R. Skovoroda, "Inverse problems of the theory of elasticity in the diagnostics of soft tissue pathologies," Preprint, *Pushchino Research Center of Russian Acad. Sci.*, Pushchino, 1992.
[30] G. E. Trahey, J. W. Allison, and O. T. Ramm Von, "Angle independent ultrasonic detection of blood flow," *IEEE Trans. Biomed. Eng.*, vol. BME-34, pp. 965–967, 1987.
[31] A. R. Skovoroda, "Diagnosis of the local pathologies in the elastic medium (3-D model)," Preprint, *Pushchino Research Center of Russian Acad. Sci.*, Pushchino, 1992.
[32] ——, "Diagnosis of the local pathologies in the elastic medium (2-D model)," Preprint, *Pushchino Research Center of Russian Acad. Sci.*, Pushchino, 1992.
[33] J. N. Goodier, "Concentration of stress around spherical and cylindrical inclusions and flaws," *Trans. ASME* , vol. 55, no. 39, pp. 39–44, 1933.
[34] M. O'Donnell, A. R. Skovoroda, and B. M. Shapo, "Measurement of arterial wall motion using Fourier based speckle tracking algorithms," *Proc. 1991 IEEE Ultrason. Symp.* , pp. 1101–1104, 1991.
[35] A. A. Samarskii and E. S. Nikolaev, *Methods of the solution of the net equations.* Moscow: Nauka, 1978.
[36] A. E. Green and J. E. Adkins, *Large elastic deformations and non-linear continuum mechanics.* Oxford: Clarendon Press, 1960.

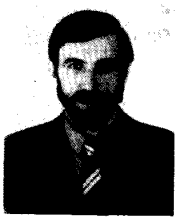

Andrei R. Skovoroda recieved the B.S. and M.S. degrees in mathematics and mechanics in 1973 and 1975, respectively, from the Novosibirsk State University, USSR, and the Ph.D. degree in 1985 from the Moscow State University, USSR.

From 1975 to 1977 he was a lecturer in Theoretical Mechanics at the College of Textile Technology, Barnaul, USSR. From 1977 to 1980 he was a Ph.D. researcher at the subfaculty of Plasticity of the Moscow State University, where he worked on the dynamic behavior of plates under blast-type loading. In 1981, he held an appointment as a Junior Research Associate with the Laboratory of Mathematical Modeling of the Research Computing Center of the USSR Academy of Sciences (presently, the Institute of Mathematical Problems of Biology, Russian Academy of Sciences), where he developed efficient mathematical methods to solve the differential equations of the theory of elasticity. In 1986 he bacame a Senior Research Associate and was Scientific Secretary at the same Institute from 1988 to 1991. He is currently Head of the Laboratory of Mathematical Problems in Biomechanics and works on the biomechanics of soft tissue.

Dr. Skovoroda is a member of the Russian Association of Experts in Ultrasonic Medical Diagnostics. He has authored and co-authored more than 40 articles for severa archival publications and papers that were presented at All-Union and International meetings.

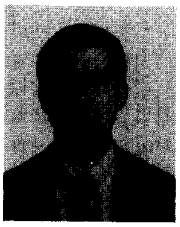

Stanislav Y. Emelianov (M'94) was born in May 1966. He received the B.S. and M.S. degrees in physics in 1986 and 1989, respectively, from the Moscow State University, and the Ph.D. degree in physics in 1993 from the Institute of Mathematical Problems of Biology of the Russian Academy of Sciences, and Moscow State University, Russia.

He is currently a Research Associate with the Laboratory of Mathematical Problems of Biomechanics at the Institute of Mathematical Problems of Biology and a Visiting Research Scientist with the Biomedical Ultrasonics Laboratory at the University of Michigan. His research interests are in the areas of modeling of tissue biomechanics, tissue characterization, and medical imaging.

Mark A. Lubinski was born in Kettering, OH on October 12, 1967. He received the B.S. degree in electrical engineering in 1990 from Carnegie-Mellon University and the M.S. degree in bioengineering in 1993 from the University of Michigan.

From 1990 to 1991 he worked as a computer engineer with the Department of Neurophysiology at Children's Hospital of Pittsburgh, PA. He is currently a National Science Foundation Graduate Fellow in bioengineering at the University of Michigan. His research interests include signal processing, medical imaging, and motion estimation.

Armen P. Sarvazyan (M'91) was born on July 2, 1939, in Erevan, Armenian Republic, USSR. He received the M.S. degree in physics from Moscow State University in 1964, the Ph.D. degree in biophysics from the Institute of Biophysics of the Academy of Sciences of the USSR in 1969, and the D.Sc. degree also from the same Institute in physics and math in 1983.

He is currently a Research Professor with Rutgers University, NJ and his permanent position is the Head of the Laboratory of Biophysical Acoustics of the Institute of Theoretical and Experimental Biophysics of the Russian Academy of Sciences, Pushchino, Russia. His research interests are acoustical properties of biological objects, thermodynamic and ultrasonic studies of biopolymers, biphysical bases of ultrasonical medical imaging, development of methods and devices for acoustical and mechanical measurements in biomedical studies. He has more than 50 patents and 200 publications in various fields of biophyics, acoustics, and biomedical engineering.

Matthew O'Donnell (M'79–SM'84–F'93) received the B.S. and Ph.D. degrees in physics from the University of Notre Dame in 1972 and 1976.

Following his graduate work, he moved to Washington University, St. Louis, MO, as a post-Doctoral Fellow in the Physics Department working on applications of ultrasonics to medicine and nondestructive testing. He subsequently held a joint appointment as a Senior Research Associate with the Physics Department and a Research Instructor of Medicine with the Department of Medicine at Washington University. In 1980 he was with General Electric Corporate Research and Development Center, Schenectady, NY, where he continued to work on medical electronics, including NMR and ultrasound imaging systems. During 1984–1985, he was a visiting fellow with the Department of Electrical Engineering, Yale University, investigating automated image analysis systems. Most recently, he has worked on the application of advanced VLSI circuits to medical imaging systems. In 1990, he became a Professor of Electrical Engineering and Computer Science at the University of Michigan, Ann Arbor. He has authored or coauthored 79 archival publications, including two receiving Best Paper awards, numerous presentations at national meetings, and 32 patent applications and 30 issued patents.

Dr. O'Donnell is a member of Sigma Xi and the American Physical Society.